Fast Prediction of the Pressure Flow Field for Cavitation Flow in Orifice Plate Based on POD-BPNN

Xing Hu, Ruiping Xiong, Zhongping Zhao, and Junhong Yang

Abstract—**This study introduces an efficient prediction method for pressure flow fields in orifice plates by integrating Proper Orthogonal Decomposition (POD) with Backpropagation Neural Networks (BPNN). The methodology begins with Latin hypercube sampling to create a wide range of operating conditions, which are then used in Computational Fluid Dynamics (CFD) simulations to generate corresponding flow field data. This data is compressed using the snapshot POD method, which extracts spatial modes and modal coefficients. A neural network is subsequently trained to map these operating conditions to the modal coefficients. For new conditions, the trained network predicts the modal coefficients, which are then combined with the base modal matrix to reconstruct the pressure flow field. Validation against CFD results demonstrates high accuracy and efficiency, with prediction errors below 2.5% across all tested conditions and computation times under 0.5 seconds.**

Index Terms—**POD-BPNN, Snapshot POD, Orifice Plate, Pressure Flow Field**

I. Introduction

Orifice Plates are widely used in fluid transport and control systems, such as in nuclear power plants and the chemical industry, to manage the fluid flow. As fluid passes through an orifice plate, upstream pressure drops, which may lead to cavitation. Cavitation occurs when vapor bubbles form and subsequently collapse, generating localized high temperatures, pressures, and high-velocity impacts. This phenomenon can induce vibrations and noise within the pipeline, contributing to pipeline fatigue and potential structural damage. Thus, predicting whether the internal fluid pressure in an orifice plate will fall below the cavitation pressure under varying operating conditions is crucial for ensuring the safe operation of fluid transport and control systems.

In recent years, Computational Fluid Dynamics (CFD) has become a critical tool, either supplementing or replacing experimental approaches for fluid flow analysis([1], [2]). For orifice plate flows, numerous studies have employed CFD to investigate flow characteristics ([4], [5], [6], [7], [8]). These studies have shown a high alignment between CFD predictions and experimental results. Some researchers have multiphase flow models in CFD to examine cavitating flows in orifice plates, reporting improved agreement between numerical and experimental results ([4], [9], [10], [11], [12]).

To predict regions in the pressure flow field of an orifice plate where pressure falls below the cavitation threshold, it is necessary to simulate multiple operating conditions within a specified range. This process typically involves solving the flow field repeatedly across different conditions, which can be computationally expensive if using full-scale CFD simulations. However, a reduced-order surrogate model could enable rapid prediction of flow field solutions across various conditions, thereby avoiding repetitive, large-scale CFD computations and enhancing computational efficiency.

The Proper Orthogonal Decomposition (POD) method is commonly applied in fluid dynamics for reduced-order modeling. It decomposes flow fields into optimal modes based on least-squares minimization, generating a set of spatial modes and associated modal coefficients that a surrogate model can approximate. As fluid problems increase in complexity, the relationship between input variables and POD-derived modal coefficients often becomes nonlinear. Neural networks are well-suited to capture these nonlinear relationships, as they can be trained to map input variables to outputs without needing explicit functional forms. Consequently, the POD-BPNN approach has garnered increasing attention in recent studies ([12], [13], [14], [15], [16], [17]).

The existing literature on POD-BPNN applications for fluid flow analysis ([17], [19]) has largely focused on classic cases, such as two-cylinder flows, with most studies centered on predicting the temporal evolution of flow fields under constant boundary conditions. This study distinguishes itself by integrating the POD method with a multilayer neural network to predict flow fields across varying boundary conditions, marking a significant advancement in applying POD techniques for flow field prediction in dynamic operational settings.

II. Orifice Plate Geometry Model

The orifice plate model in this study aligns with the thick orifice plate model described in [6]. A three-dimensional geometric representation of this thick orifice plate is illustrated in Fig. 1. Key dimensions include the length L=69.85[mm], the inner diameter $d_0 = 6.35[mm]$, the

Manuscript received August 15, 2024; revised December 5, 2024.

Xing Hu is a postgraduate student of the School of Mechanical Engineering, Sichuan University, Chengdu, China (e-mail: 2022223025110@stu.scu.edu.cn).

Ruiping Xiong is an associate professor at the School of Mechanical Engineering, Sichuan University, Chengdu, China (corresponding author to provide phone: +8613550002782; e-mail: xiongruiping214@outlook.com).

Zhongping Zhao is a postgraduate student of the School of Mechanical Engineering, Sichuan University, Chengdu, China (e-mail: zhaozhongping@stu.scu.edu.cn).

Junhong Yang is a postgraduate student of the School of Mechanical Engineering, Sichuan University, Chengdu, China (e-mail: 2022223025083@stu.scu.edu.cn).

outside diameter $d_1 = 28.5[mm]$, and the length of the throttling section $L_0 = 12.7[mm]$.

To ensure the accuracy of the CFD simulation, both upstream and downstream portions of the orifice plate piping are incorporated. Specifically, the upstream pipe length is set to $6L_0$, and the downstream pipe length to $20L_0$, allowing for a more accurate representation of fluid dynamics across the orifice plate. Fig. 2 depicts the overall 2D fluid domain, including the upstream and downstream sections surrounding the thick orifice plate.

A. CFD Calculation Model

For the CFD simulations in this study, Fluent 2020R2 was utilized. The boundary conditions employed were pressure-inlet and pressure-outlet, with the pressure-inlet values ranging from 1500 to 5500 psi(consistent with the values used in [9] for subsequent comparisons). The pressure-outlet values were set to 0.1 to 0.8 times the corresponding pressure-inlet values.

To simplify the CFD calculations, an axisymmetric model was implemented. The materials considered in the simulation included liquid water as the primary phase and water vapor as the secondary phase, with the flow assumed to occur at a temperature of 300 K. Convergence criteria for all residuals during the simulation were established at 1e-05. Additional parameter settings for the simulation model are detailed in Table 1. An unstructured mesh was employed to discretize the fluid domain, as illustrated in Fig. 3.

B. Grid Independence Verification

The accuracy of CFD solution results is influenced by the number of meshes used in the simulation[19]. To ensure numerical accuracy while minimizing computational time, a grid independence verification was conducted with different mesh densities for the thick orifice plate: 25,593, 53,357, 105,550, and 203,249 cells.

Each meshing model was simulated under identical conditions, and the resulting pressure and velocity distributions along the axis were compared across the different flow fields. As illustrated in Fig. 4, the results from the four mesh densities exhibited a high degree of consistency with minimal error. Therefore, it was determined that the CFD model's solution results within the mesh range of 25,593 to 203,249 cells are independent of the mesh density. Consequently, a mesh model with 53,357 cells was selected for all CFD simulations in this study, excluding those related to grid independence verification.

C. CFD Model Reliability Validation

To validate the accuracy of the CFD calculation model presented in this study, the numerical simulation results were compared with existing literature [9]. The axial pressure distribution obtained from the CFD calculations for the orifice plate at various pressure ratios was compared to the results from the literature using a fixed inlet pressure of 5000 psi. As shown in Fig. 5, the CFD model results strongly agreed with those from the literature, demonstrating the reliability of the CFD model utilized in this study.

III. Fast Prediction Method For Pressure Flow Field

To enable rapid prediction of the pressure flow field for the orifice plate under varying operating conditions, the process begins with sampling the parameter space using the Latin hypercube sampling method. Subsequently, the sampled flow field solutions are downscaled utilizing the snapshot POD method. Finally, a BPNN model is employed to capture the nonlinear relationship between the input operating conditions and the output modal coefficients.

A. Latin Hypercube Sampling Method

Latin Hypercube Sampling (LHS), introduced by McKay in the 1970s [20], is a stratified sampling technique that ensures an even distribution of samples across the input space. In LHS, each input random variable is first sampled, followed by a rearrangement of sampled values to minimize correlations among them. Compared to random sampling methods, LHS produces a more uniformly distributed sample set and can capture sample points at lower probability densities with fewer samples. In CFD optimization problems utilizing surrogate models, LHS is commonly applied to construct representative sample pools efficiently.

B. POD Method

The POD method uses a set of reduced-order bases to provide an optimal low-dimensional approximation of data in high-dimensional, nonlinear spaces. Traditional POD achieves data reduction through eigenvalue decomposition of the data matrix. Since eigenvalue decomposition applies only to square matrices, it is necessary to construct a covariance matrix R for eigenvalue decomposition when dealing with non-square matrices. An alternative approach to achieve POD decomposition is Singular Value Decomposition (SVD) [21]:

$$A = U\Sigma V^T \tag{1}$$

Where A is the data matrix to be downscaled. The matrix's singular values, arranged on the diagonal, form the modal matrix and the corresponding modal coefficient matrix.

The conventional POD method requires solutions over the entire domain, which is computationally intensive for high-dimensional problems and may result in reduced accuracy and stability. The snapshot POD method [22] addresses these issues, enabling efficient extraction of optimal modes by constructing a snapshot matrix from the flow field solutions of sampled conditions:

$$U_{cp} = \begin{bmatrix} u(c_1,p_1) & u(c_1,p_2) & \cdots & u(c_1,p_M) \\ u(c_2,p_1) & u(c_2,p_2) & \cdots & u(c_2,p_M) \\ \vdots & \vdots & \ddots & \vdots \\ u(c_N,p_1) & u(c_N,p_2) & \cdots & u(c_N,p_M) \end{bmatrix} \tag{2}$$

Where U_{cp} is the snapshot matrix of the flow field, N is the number of operating conditions, and M represents the number of grid nodes. Each row of the matrix corresponds to a specific pressure flow field solution under a given condition. The snapshot matrix can be decomposed into an average matrix and a fluctuation (pulsation) matrix:

$$U_{cp} = \bar{U}_{cp} + \tilde{U}_{cp} \tag{3}$$

$$\vec{\varphi} = \left[\frac{\sum_{i=1}^{N} u(c_i, p_1)}{N} \quad \frac{\sum_{i=1}^{N} u(c_i, p_2)}{N} \quad \cdots \quad \frac{\sum_{i=1}^{N} u(c_i, p_M)}{N} \right] \tag{4}$$

$$\bar{U}_{cp} = \begin{bmatrix} \vec{\varphi} \\ \vec{\varphi} \\ \vdots \\ \vec{\varphi} \end{bmatrix}_{N\times 1} \tag{5}$$

Where $\bar{U}_{cp}$ is the average matrix, $\tilde{U}_{cp}$ is the pulsation matrix, and $\vec{\varphi}$ represents the average value of the flow field solutions across various conditions. By reducing the dimensionality of the pulsation matrix instead of the original matrix, computational costs are further minimized. To reduce the dimensionality of the pulsation matrix, the optimal low-dimensional solution is sought in the least squares sense:

$$min\sum_{i=1}^{N} \| \tilde{U}_{cp} - \Phi\Phi^{\mathrm{T}}\tilde{U}_{cp} \|, \Phi^{\mathrm{T}}\Phi = I \tag{6}$$

Where Φ is the orthogonal base set that provides the optimal low-dimensional solution. Each mode in the modal matrix aligns with a singular value in the diagonal matrix, and the squared singular value of a mode termed its energy value reflects the impact of that mode on the reconstructed matrix. During reconstruction, modes with smaller energy values are omitted, with only the highest-energy modes and their corresponding coefficients retained for reconstructing the pulsation matrix, significantly reducing the number of modal coefficients required for BPNN prediction. In SVD decomposition, modal energies are calculated as follows:

$$E = \sum_{i=1}^{m} \sigma_i^2 \tag{7}$$

$$k_i = \frac{\sigma_i^2}{E} \times 100\% \tag{8}$$

$$k_{sum} = \sum_{j=1}^{i} k_i \tag{9}$$

Where m is the number of singular values. E represents the cumulative energy of all modes, k_i is the energy proportion of the i-th mode, and k_{sum} is the cumulative proportion of the first i-th modes' energy. When k_{sum} exceeds a specific threshold, the pulsation matrix can be accurately approximated by the first i-th modes, allowing the remaining modes to be discarded, as illustrated in Fig. 6.

C. BPNN Network Architecture

The Back Propagation neural network (BPNN) is one of the most widely used neural network models, featuring an architecture that includes one input layer, one or more hidden layers, and a single output layer. While BPNN is effective, traditional implementations face challenges such as slow convergence speeds, a tendency to get trapped in local optima, and limited generalization capabilities. To mitigate these issues, various optimization techniques have been proposed, with the Levenberg-Marquardt (LM) algorithm being a notable enhancement known as LM-BPNN. This method iteratively optimizes the BPNN's weights and biases.

This study employed the LM-BPNN to model the relationship between input operating conditions and the corresponding modal coefficients. The designed neural network consists of five layers: one input layer, three hidden layers, and one output layer, as illustrated in Fig. 7. The dataset comprises 976 samples, which were partitioned into a training set, a test set, and a validation set in a ratio of 7:2:1. Fig. 8 depicts the overall workflow for the POD-BPNN methodology, outlining the integration of POD with BPNN for efficient prediction of pressure flow fields under varying conditions.

IV. Results And Discussion

A. Latin Hypercube Sampling Results

976 samples were obtained by sampling in the working condition sample space using the Latin Hypercubic Sampling method, and some of the sample points are shown in Table 3.

B. POD Decomposition Results

CFD simulations were performed across 976 operating conditions to capture the corresponding pressure flow fields, forming a snapshot matrix. This matrix underwent POD decomposition to extract modes and their respective modal coefficients, resulting in 976 modes. The modal energy values were calculated, and the cumulative energy of the first 30 modes is displayed in Fig. 10. Notably, with just the first 20 modes, the cumulative energy reached 99.9999% of the total energy. Thus, these 20 modes are sufficient to reconstruct the flow field with high accuracy, allowing us to discard higher-order modes and focus only on the modal coefficients of these first 20 modes for BPNN training.

Fig. 9 illustrates the first 20 modes obtained from the POD for the pressure flow field around the orifice plate under specific operating conditions. Each mode captures unique flow field structures, with the first and second modes prominently showcasing large-scale flow characteristics common in CFD results. Specifically, the first mode emphasizes primary vortex structures near the wall region of the orifice plate, reflecting the dominant flow behavior. The second mode portrays a characteristic pressure decrease across the orifice plate.

For the remaining higher-order modes (modes 3–20), we observe numerous, smaller-scale vortex structures within the wall region, representing the finer flow dynamics surrounding the orifice plate. As the modal order increases, the number of vortices near the orifice plate wall gradually increases, reflecting the instability of the flow process within the orifice plate. As shown in Fig. 9 (c)-(t), with the increase in modal order, the number of vortices on the wall gradually increases while the volume of individual vortices gradually decreases. As to the contour plots for individual modes, they reveal that high-pressure vortex regions and low-pressure vortex regions are arranged alternately. Due to the small singular values corresponding to these modes, the flow field characteristics of the orifice plate are still dominated by the first-order and second-order modes.

However, these additional modes contribute critical details, offering a more comprehensive perspective on the flow patterns and enhancing the fidelity of the overall flow field reconstruction.

C. Results Predicted By The POD-BPNN Method

To assess the accuracy and efficiency of the POD-BPNN method, we randomly selected 12 additional working conditions from the original sample space, as detailed in Table 2. Pressure flow fields for these conditions were calculated using both CFD simulations and the POD-BPNN method. The computational results are presented in Figs. 12 through 23, each containing four subplots for enhanced clarity. Subplots (a) and (b) are contour plots providing a vivid representation of flow field structures: subplot (a) displays the pressure flow field as computed by CFD, while subplot (b) shows the corresponding flow field predicted by POD-BPNN. Both use a unified color scale to directly compare structural differences between the CFD and POD-BPNN results.

Subplot (c) presents isoline highlighting numerical value distributions across the flow field. Although isoline contours may not illustrate flow structure as intuitively as contour plots, they distinctly outline the numerical distribution, with colored lines representing CFD isocurves and black lines indicating those from the POD-BPNN. This color distinction enables an effective visual comparison between the two methods, illustrating any minor deviations in magnitude at corresponding flow field positions.

To quantify differences, we calculated the relative error $e_{relative}$ at each node and the average relative error $\overline{e}_{relative}$ across all nodes, as shown below:

$$e^i_{relative} = \sqrt{(\frac{p^i_{prediction} - p^i_{CFD}}{p^i_{CFD}})^2} \times 100\%, if or nodes(i) \quad (10)$$

$$\overline{e}_{relative} = \frac{\sum_{i=1}^{n} e^i_{relative}}{n} \quad (11)$$

Subplot (d) then maps the relative error distribution across the flow field, comparing POD-BPNN predictions to CFD results.

Figs. 12 through 23 illustrate that subplots (a) and (b) align closely, with the POD-BPNN method accurately reproducing CFD-derived flow field structures across all selected conditions. The POD-BPNN predictions consistently capture pressure reduction trends in regions of abrupt cross-sectional changes, as well as low-pressure vortex regions near walls and downstream flow field changes. When the pressure ratio decreases to a certain threshold, the low-pressure vortex on the wall will further develop and begin to extend across the entire constricted area. The POD-BPNN method can accurately predict this phenomenon. As shown in Fig. 14 (a), the low-pressure area represented by the blue region does not manifest as a vortex attached to the wall but instead forms a segment within the constricted area of the orifice plate that is entirely filled with low-pressure blue regions. Fig. 14 (b) demonstrates that the pressure flow field predicted by the POD-BPNN method under extreme conditions remains consistent with the results predicted by CFD simulations.

In subplot (c), isoline contours demonstrate high consistency in value distribution between POD-BPNN and CFD results. While some deviations appear between POD-BPNN and CFD isocurves, these are generally minor and indicate only slight discrepancies in magnitude. The overall shape and trend of isocurves between CFD and POD-BPNN remain consistent, reinforcing their alignment in flow field structure predictions.

Subplot (d) highlights that relative errors tend to be higher near narrow cross-sectional areas and lower in regions with larger cross-sections. Specifically, the distribution characteristics of relative error are closely related to the low-pressure regions of the orifice plate. As shown in Figs. 12, 13, and 15 to 23, the pressure values in the vortex regions near the orifice plate wall are relatively lower, and correspondingly, the relative error of the POD-BPNN method is also higher in these vortex regions. Moreover, the shape and position of these vortices are roughly consistent with those in the pressure contour plots. In Fig. 14 the low-pressure region extends to a specific section of the orifice plate, and the region with higher relative error also extends to this section. Higher pressure ratios between outlet and inlet show lower error rates, while smaller pressure ratios lead to larger errors in narrow areas, suggesting slightly reduced accuracy for the POD-BPNN method under extreme flow conditions.

The relative error contour plot primarily illustrates trends and patterns in relative errors. For a more quantitative representation, boxplots of relative errors for each of the 12 working conditions were generated, as shown in Figs. 27 and 28. These reveal that, for all conditions, the mean relative error of the POD-BPNN method remains below 2.5%. Additionally, the interquartile range (IQR) is relatively close to the mean, indicating consistency. However, outliers are present beyond the whiskers of some boxplots, with notably large values. For example, in sample condition 3, the mean value extends beyond the box due to the influence of these outliers.

To further characterize relative error distribution, Table 4 presents the mean, median, standard deviation, and IQR for each sample. Most samples show close mean and median values, along with small standard deviations, suggesting that the mean effectively represents the error level in POD-BPNN results. In sample condition 3, however, the high standard deviation and noticeable difference between the median and mean reflect greater data dispersion, highlighting the impact of outliers on the mean. In this case, the median better represents the POD-BPNN error, reaffirming that prediction accuracy decreases in more challenging flow conditions.

In addition, we investigated the impact of various operating conditions on the error of the POD-BPNN method during testing. Fig. 24 illustrates the trend of the average and median errors of the POD-BPNN method as the pressure ratio at the outlet and inlet of the orifice plate varies. The figure shows that when the pressure ratio at the outlet and inlet is either low or high, the error of the POD-BPNN method is relatively larger compared to when the pressure ratio is moderate. This indicates that the POD-BPNN method has higher predictive accuracy for situations with a

moderate pressure ratio. Fig. 26 depicts the trend of the average and median errors of the POD-BPNN method as the pressure difference across the orifice plate changes. With the increase in the pressure values at both ends, the average and median errors do not exhibit a clear trend, suggesting that the pressure interpolation is not significantly related to the pressure difference between the two ends. Fig. 25 presents the trend of the average and median errors of the POD-BPNN method as the inlet pressure of the orifice plate varies. Similarly, as the inlet pressure increases, the average and median errors do not show a clear trend, indicating that the inlet pressure is not a major factor affecting the error. Integrating the previous comparisons and discussions, it can be concluded that the accuracy of the POD-BPNN method in this study is primarily influenced by the pressure ratio between the outlet and inlet pressures.

Contour plots from CFD calculations offer a clear and intuitive depiction of flow field structure, aiding understanding flow development trends and internal conditions. Beyond contour plots, CFD provides rigorous quantitative analysis by extracting numerical values from specific flow field regions. A critical aspect of CFD calculations for orifice plates is illustrating pressure drop characteristics, typically through axial pressure distribution within the pressure flow field. To evaluate the POD-BPNN method's accuracy and practicality comprehensively, we have also plotted axial pressure distribution curves for the orifice plate as determined by both CFD and the POD-BPNN method.

In Fig. 29, the left side shows axial pressure distribution curves from CFD calculations under the 12 working conditions, while the right side presents POD-BPNN results. For easier comparison, Figs. 30 and 31 plot both methods' results on the same coordinate system for each sample, with blue for CFD and red for POD-BPNN. The results show that axial pressure distributions predicted by POD-BPNN closely align with CFD outcomes across all conditions, accurately capturing the sharp pressure drop along the axis and the partial recovery afterward.

To assess computational efficiency, Table 5 compares the processing times of the two methods for the 12 samples. CFD computation time reflects the solver's convergence duration, while POD-BPNN time includes neural network inference and vector operations. Calculations were performed in a Windows 11 environment with 16 GB RAM and an AMD Ryzen 5 5600G processor. Table 6 demonstrates that POD-BPNN computation times do not exceed 0.5 seconds per sample, showing a significant efficiency gain over CFD with computational times reduced by several orders of magnitude.

V. Conclusion

This study developed the POD-BPNN method based on CFD results to rapidly predict the pressure flow field in orifice plates. The following conclusions were drawn:

(1) After employing POD method to decompose the snapshot flow field, a multitude of modes is obtained, each with its corresponding singular value. These singular values can be utilized to calculate the energy of the modes, which in turn reflects the significance of the modes in reconstructing the flow field. Based on this principle, it is possible to discard the majority of modes and reconstruct the flow field using only the remaining modes. The number of modes to retain can be determined based on the cumulative energy of these modes. In this study, we retained modes that account for a cumulative energy of 99.9999%, which corresponds to the first twenty modes.

(2) The modes used for reconstructing the flow field, when multiplied by their corresponding specific modal coefficients and summed, can yield a specific flow field. After decomposing the snapshot flow field, multiple sets of modal coefficients can be obtained, with each set corresponding to different conditions. In this study, each set of modal coefficients corresponds to different working conditions of the orifice plate. Due to the presence of multiple modal coefficients and their corresponding conditions, a neural network can be employed as a surrogate model, leveraging its strong fitting capabilities to model the relationship between different conditions and their respective modal coefficients. Such a surrogate model is purely data-driven, making it more flexible and universal. In this study, the POD-BPNN method has demonstrated high accuracy and low computational time when predicting the pressure flow fields under different operating conditions of the orifice plate.

(3) In the existing research on the combination of POD with neural networks for predicting flow fields, most literature focuses on flow fields that change over time and predicts the flow field results at future moments. In these studies, different modal coefficients correspond to different time points. However, in this study, the snapshot flow field is composed of steady-state flow fields under various working conditions, which means that different modal coefficients correspond to different working conditions. The results of this study indicate that the POD-BPNN method is not only applicable for predicting flow fields that change over time but also effectively predicts the flow field results for specific objects under different operating conditions.

In summary, the POD-BPNN approach has shown promising accuracy and efficiency, offering a novel framework for applying POD-BPNN under complex working conditions. This advancement contributes to the field of nonlinear flow field prediction, providing a valuable tool for fast and accurate analysis in complex scenarios.

References

[1] Xinyun Liu, Dalin Wu, and Jian Hou, "Numerical Analysis of 100mm Naval Gun Barrel Composite Cooling Based on Multiphase Flow," Engineering Letters, vol. 28, no. 3, pp. 949–959, 2020.

[2] S. M. Kwa and S. M. Salim, "Numerical Simulation of Dispersion in an Urban Street Canyon: Comparison between Steady and Fluctuating Boundary Conditions," Engineering Letters, vol. 23, no. 1, pp. 55–64, 2015.

[3] O. A. P. Cappa, T. V. R. Soeira, A. L. A. Simões, G. B. Lopes Junior, and J. C. de Souza Inácio Gonçalves, "Experimental and computational analyses for induced cavitating flows in orifice plates," *Braz. J. Chem. Eng.*, vol. 37, no. 1, pp. 89–99, Mar. 2020.

[4] M. A. Mehmood, M. A. Ibrahim, A. Ullah, and M. H. Inayat, "CFD study of pressure loss characteristics of multi-holed orifice plates using central composite design," *Flow Meas. Instrum.*, vol. 70, p. 101654, Dec. 2019.

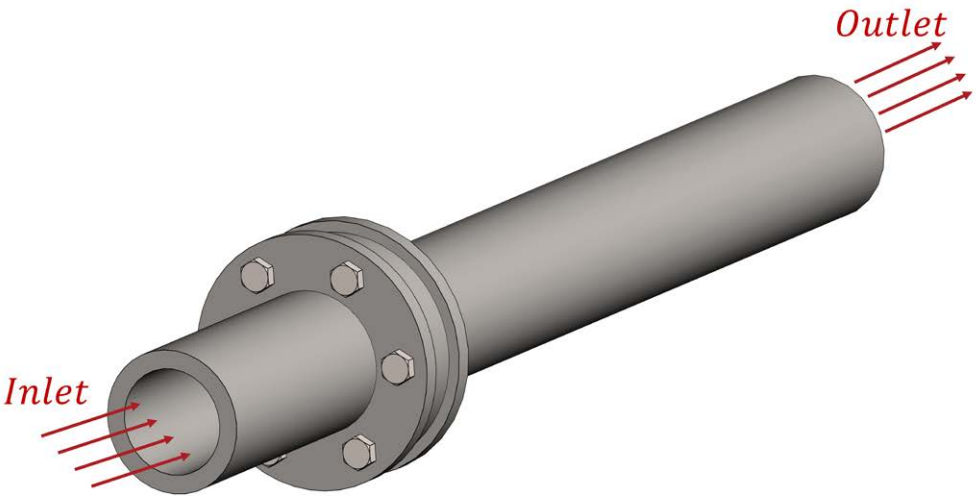

Fig. 1 3D model of the orifice plate

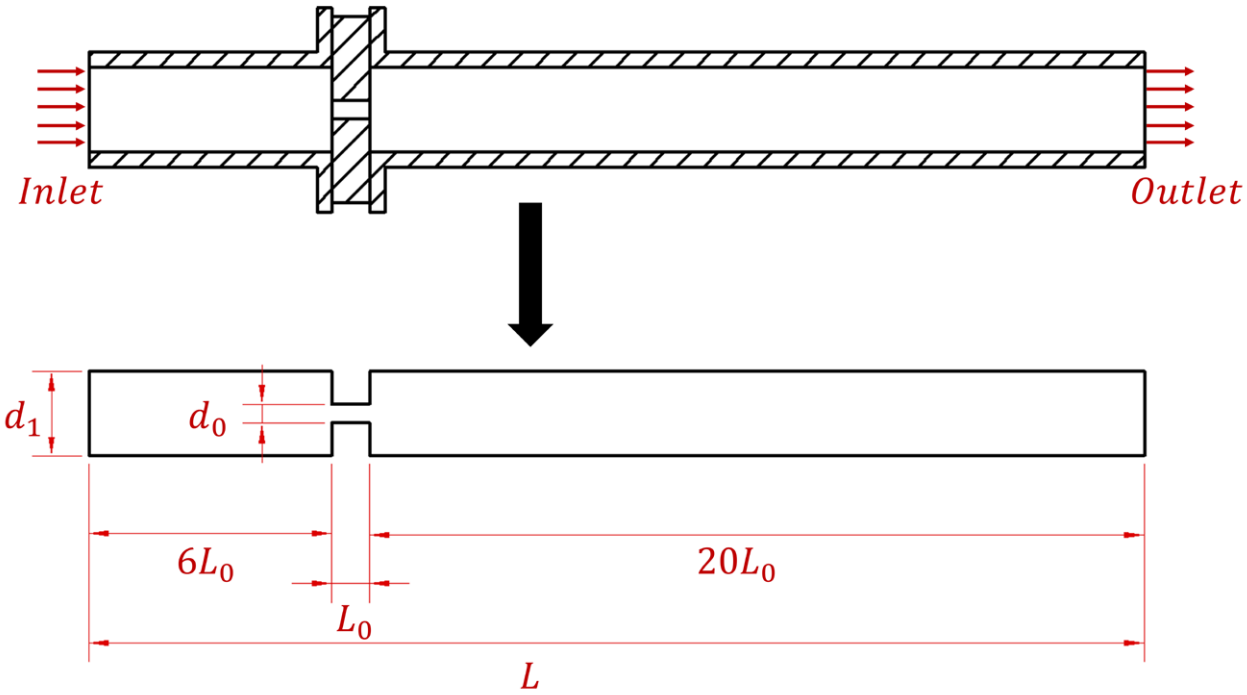

Fig. 2 Geometrical model and computational domain of the orifice plate

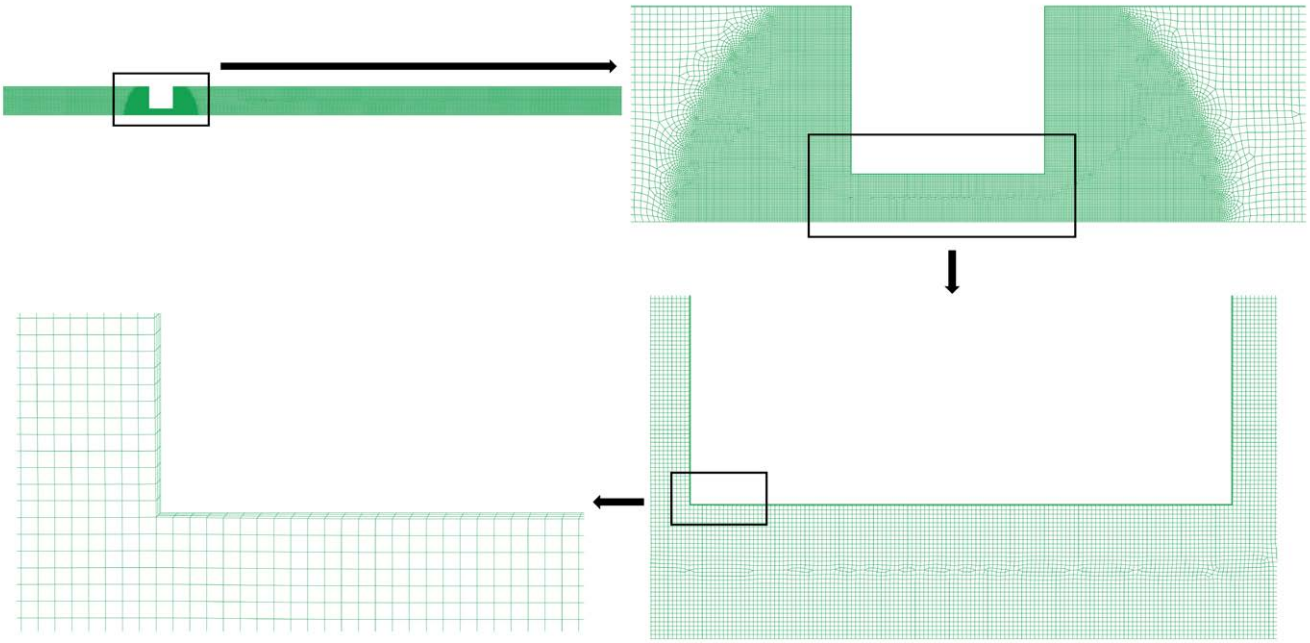

Fig. 3 Results of the mesh generation for the computational domain of the orifice plate

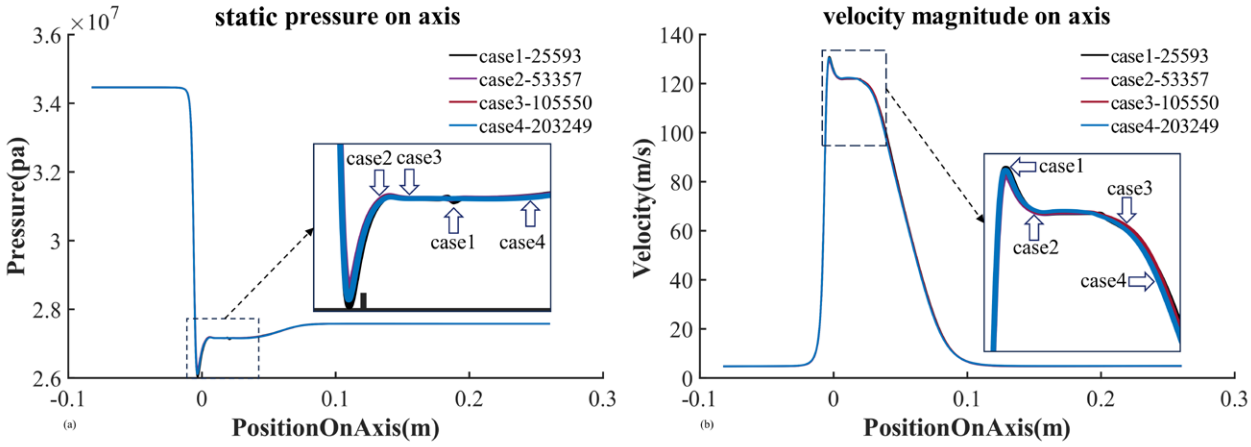

Fig. 4 Results of the grid independence verification

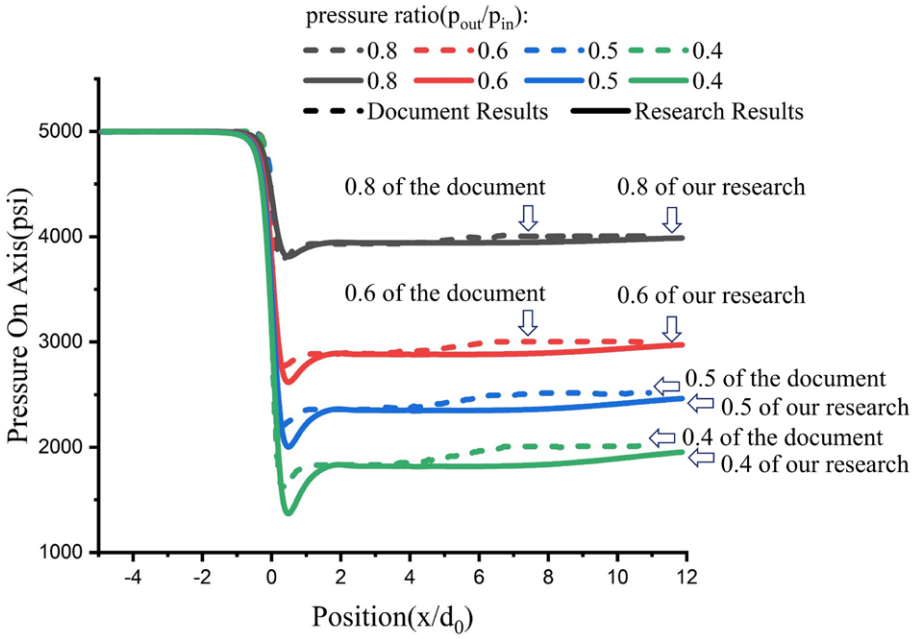

Fig. 5 Comparison of the results of this paper with the results of the reference

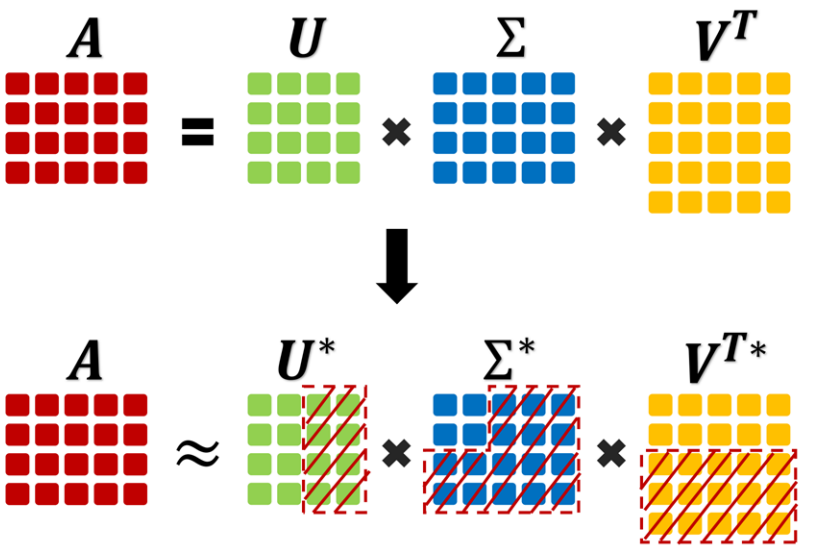

Fig. 6 The principle of the POD method

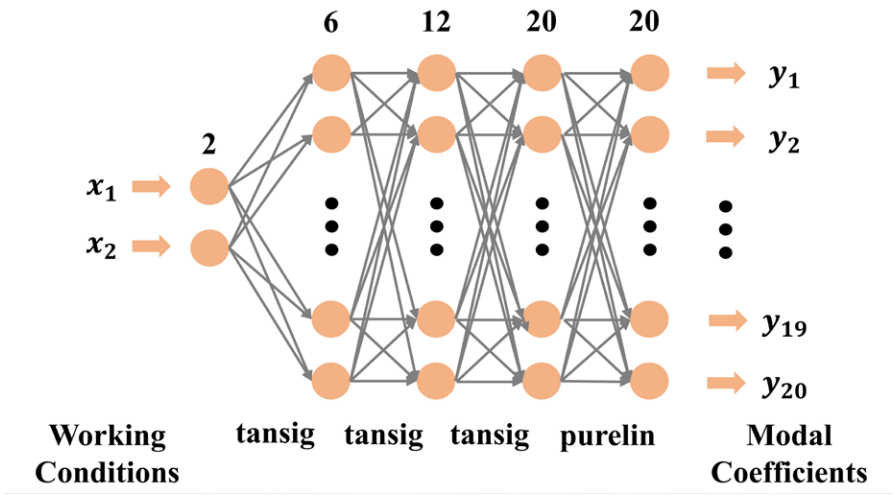

Fig. 7 Structure of the neural network

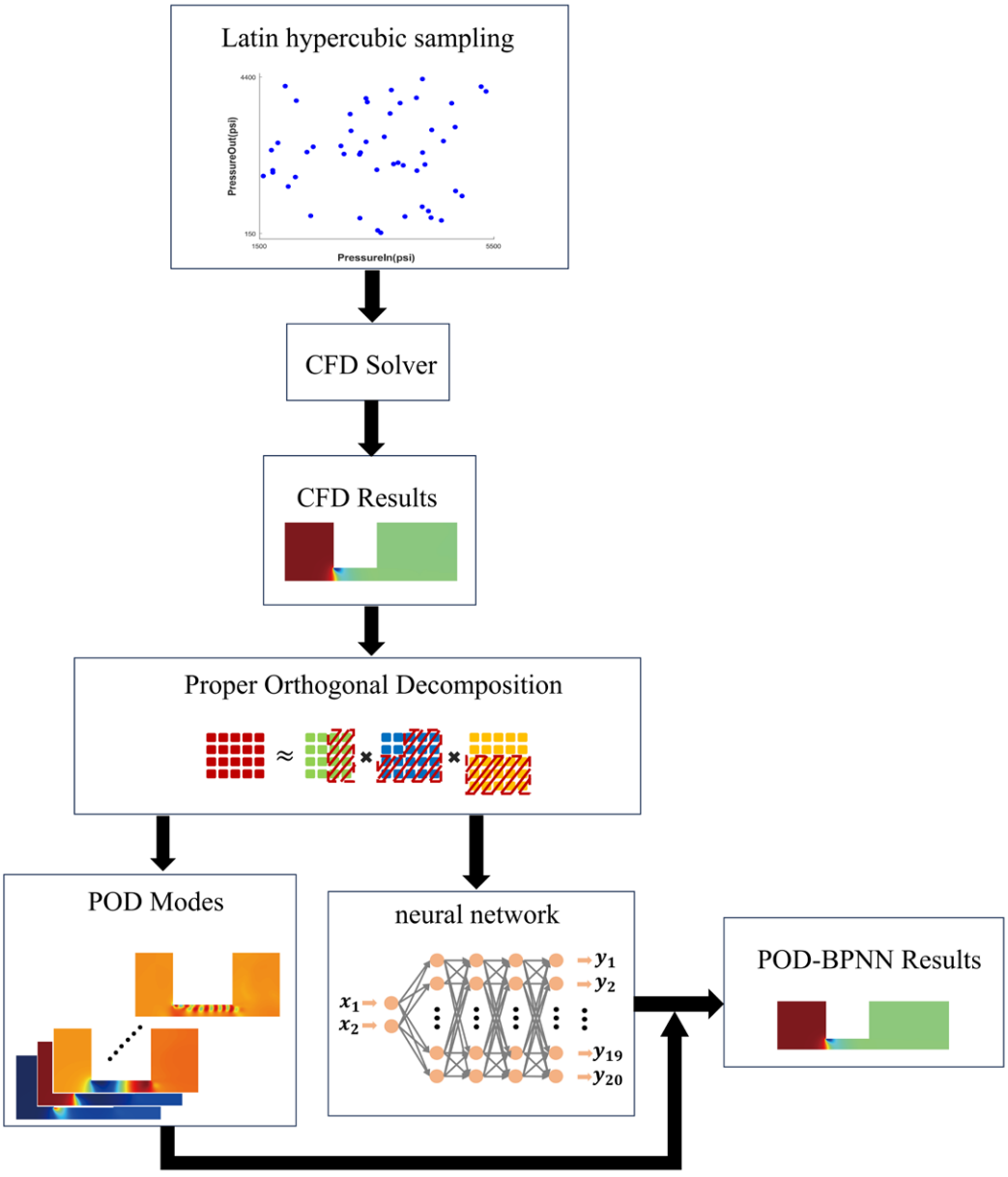

Fig. 8 Flowchart of the POD-BPNN method

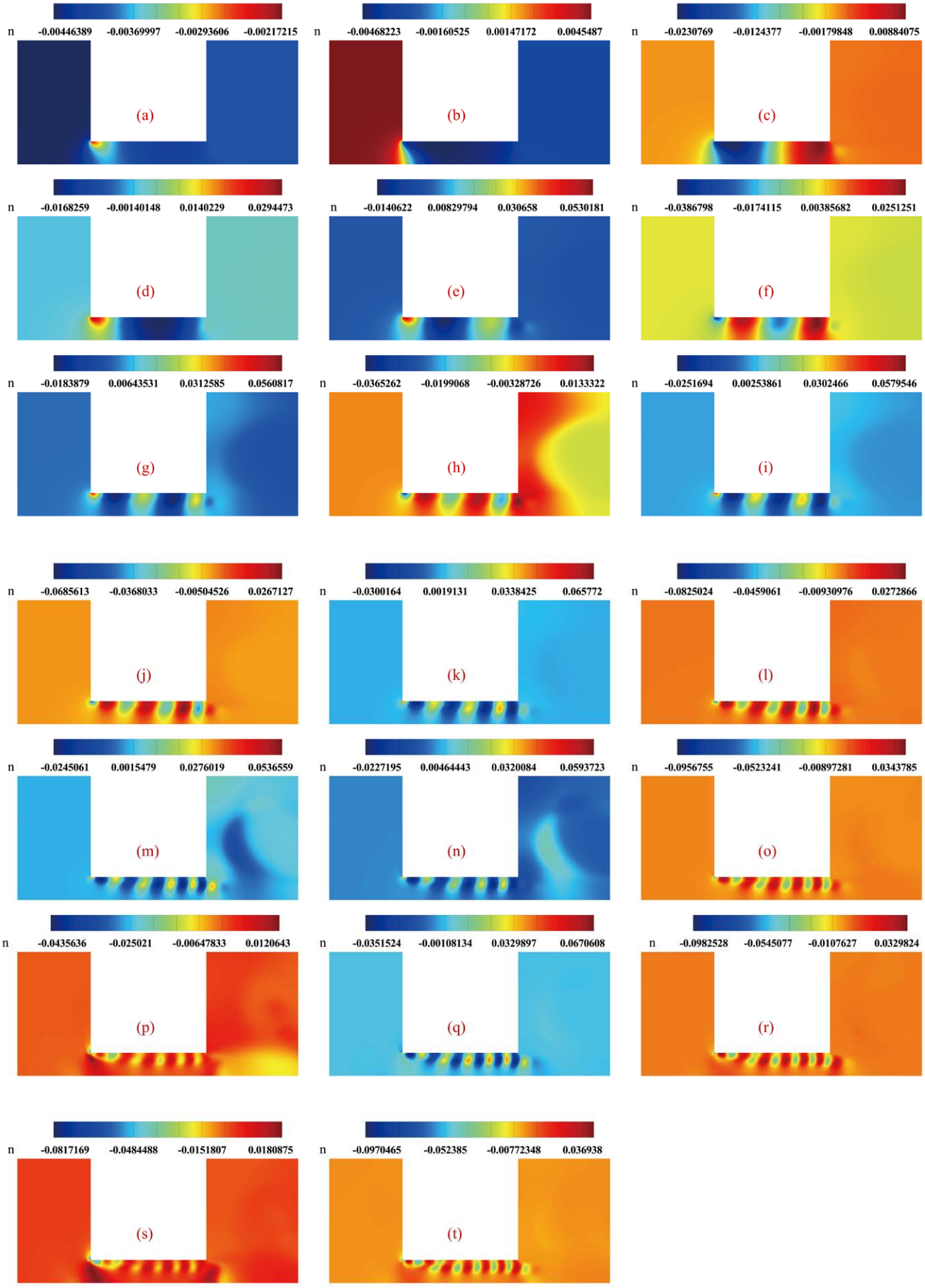

Fig. 9 Contour plots of the first 20 modes

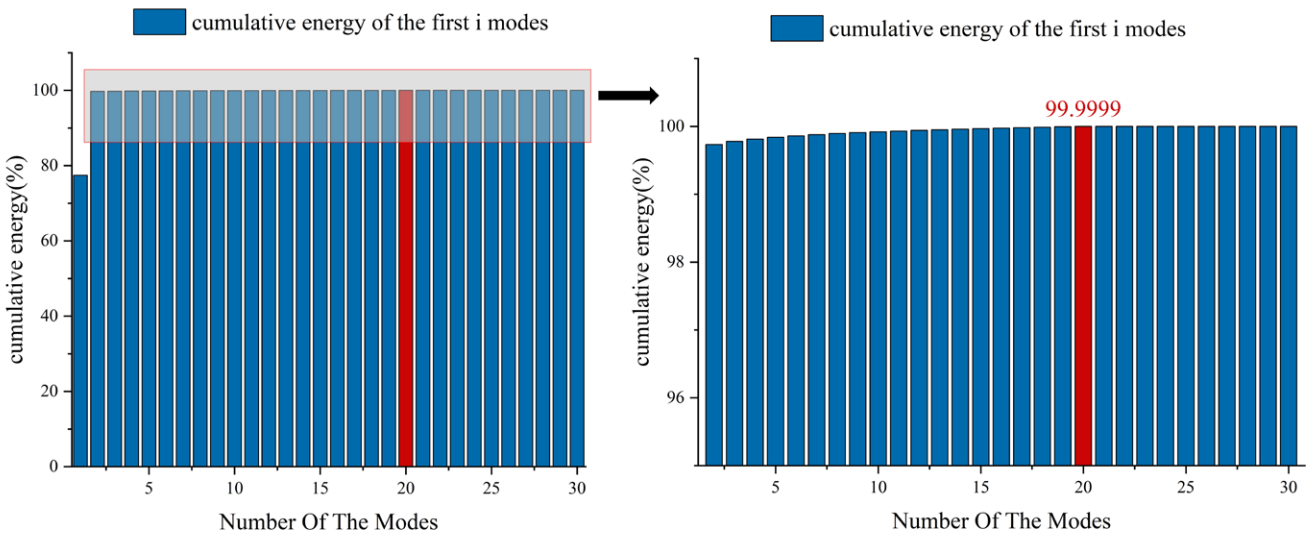

Fig. 10 Cumulative energy of the first 20 modes

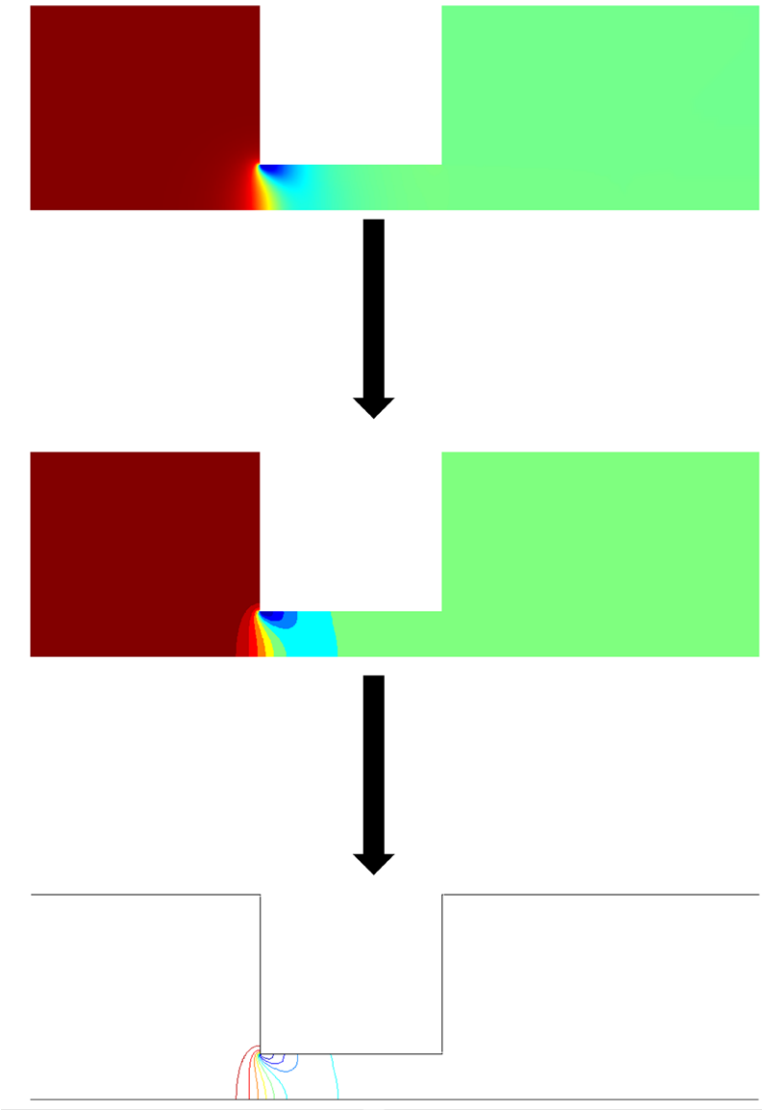

Fig. 11 The relationship between color-filled contour plot and contour map

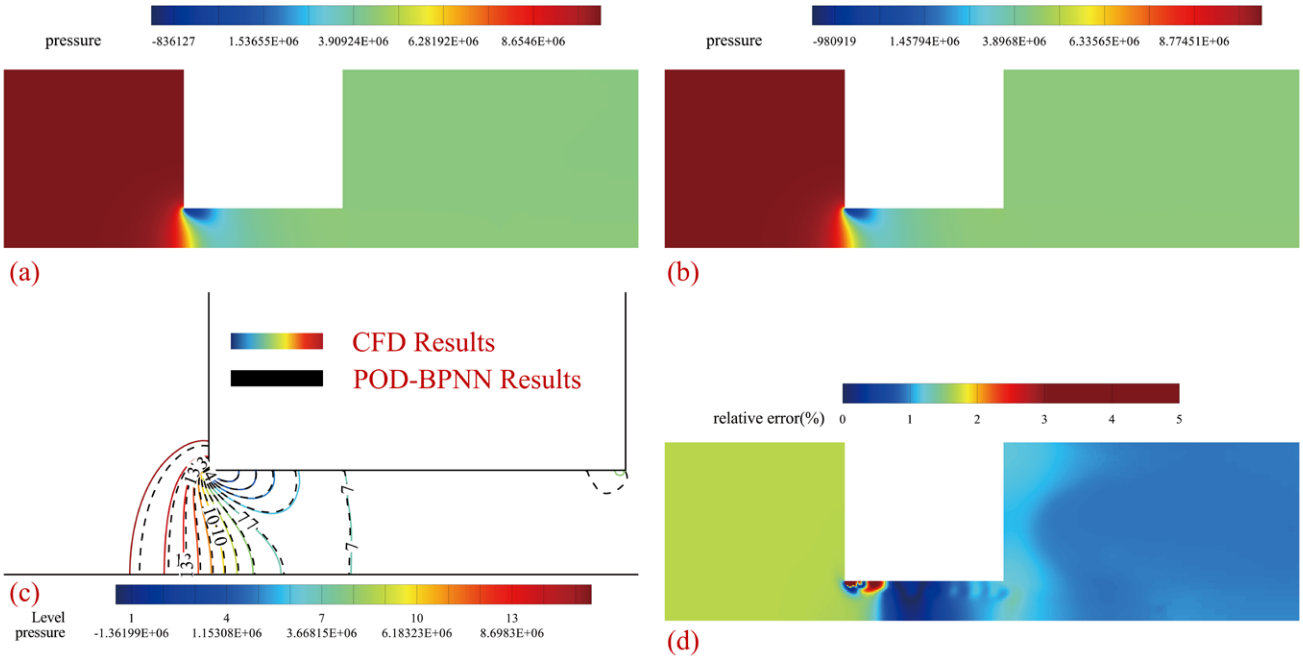

Fig. 12 Results of sample 1

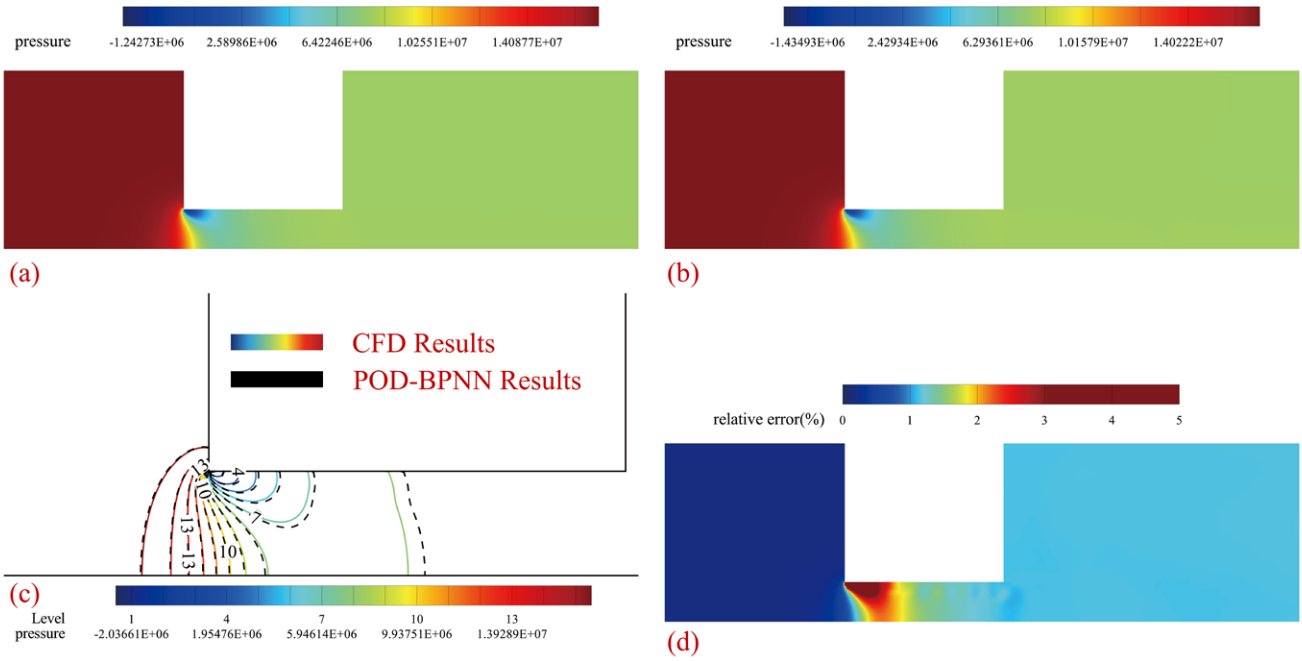

Fig. 13 Results of sample 2

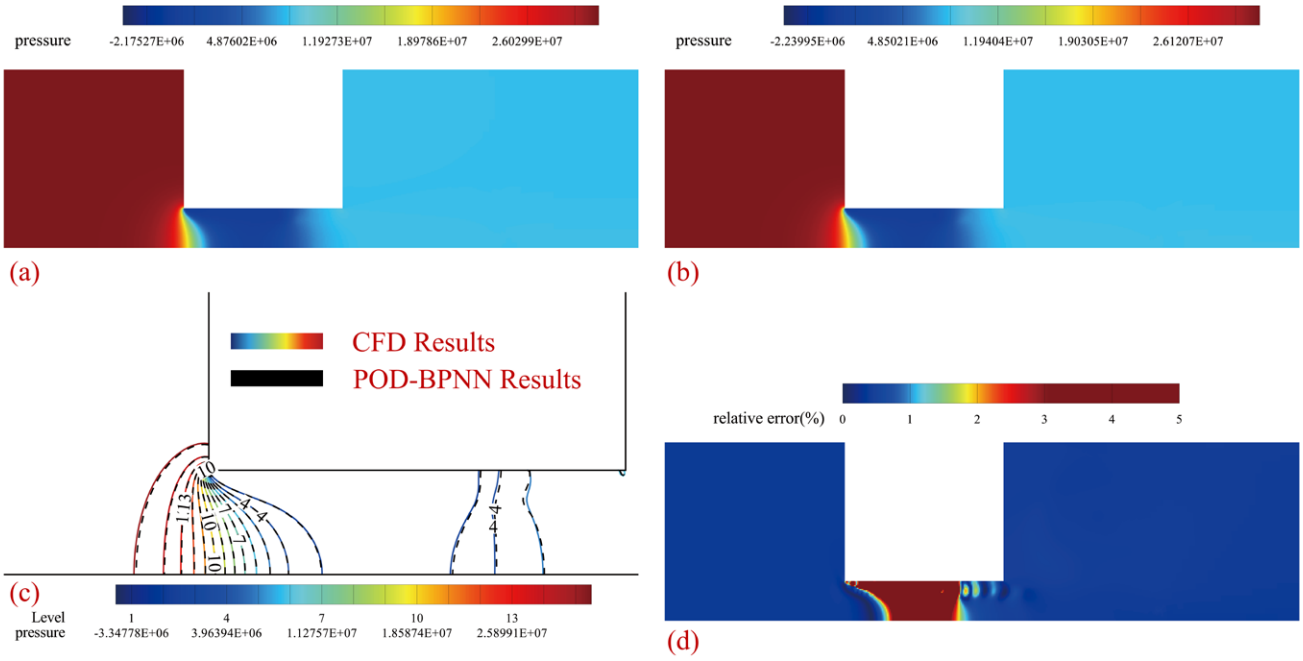

Fig. 14 Results of sample 3

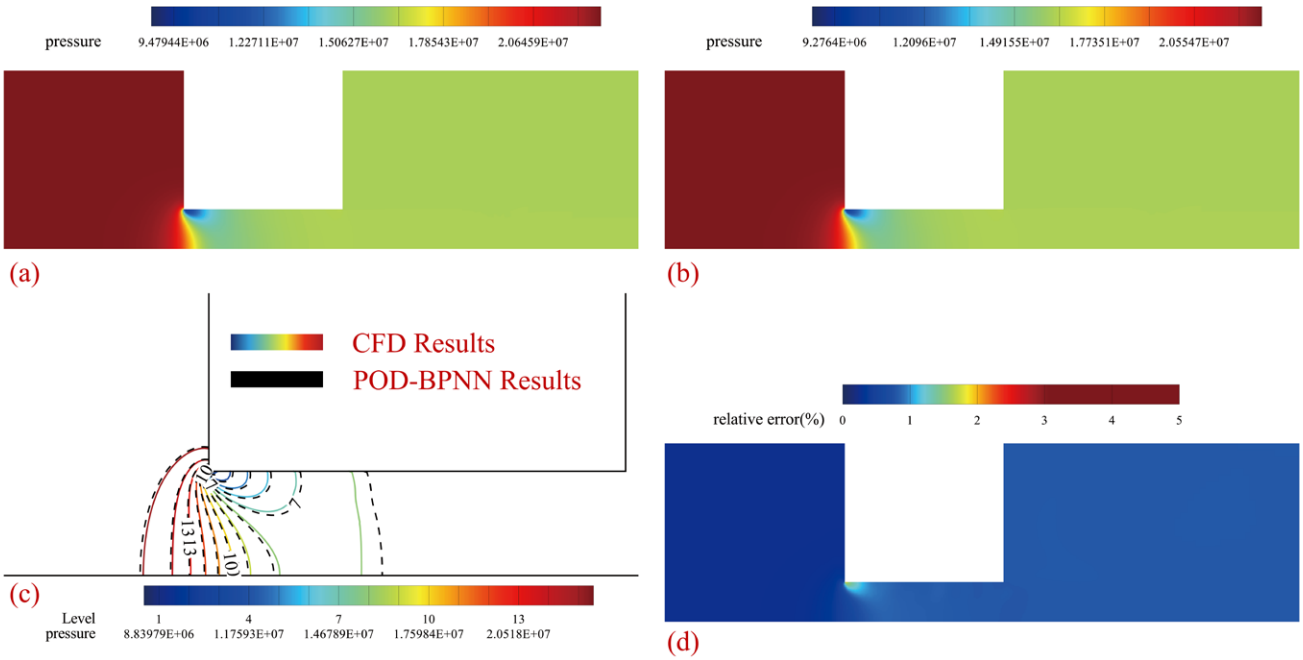

Fig. 15 Results of sample 4

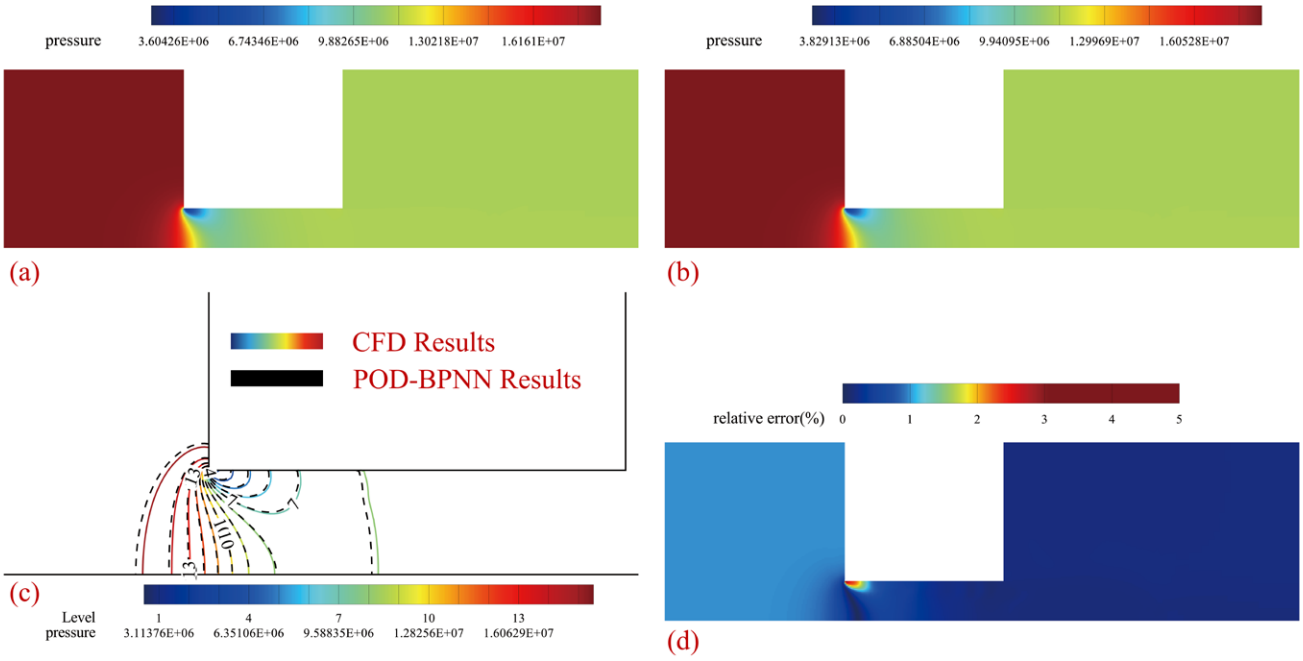

Fig. 16 Results of sample 5

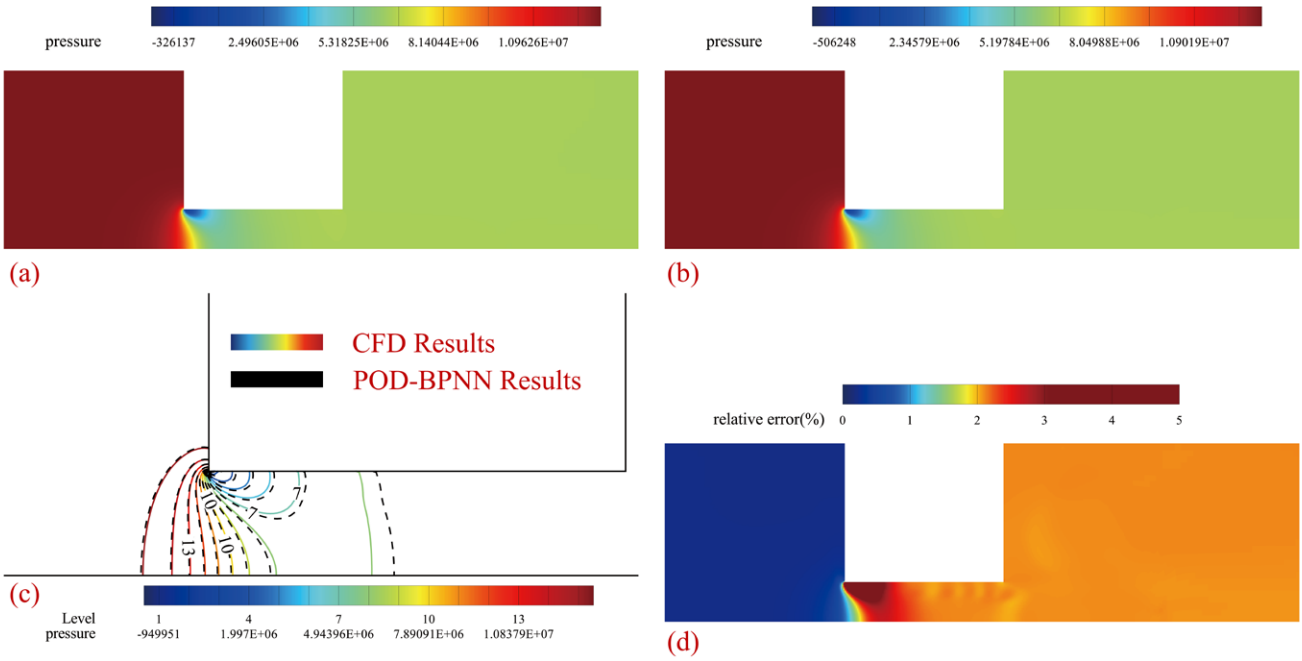

Fig. 17 Results of sample 6

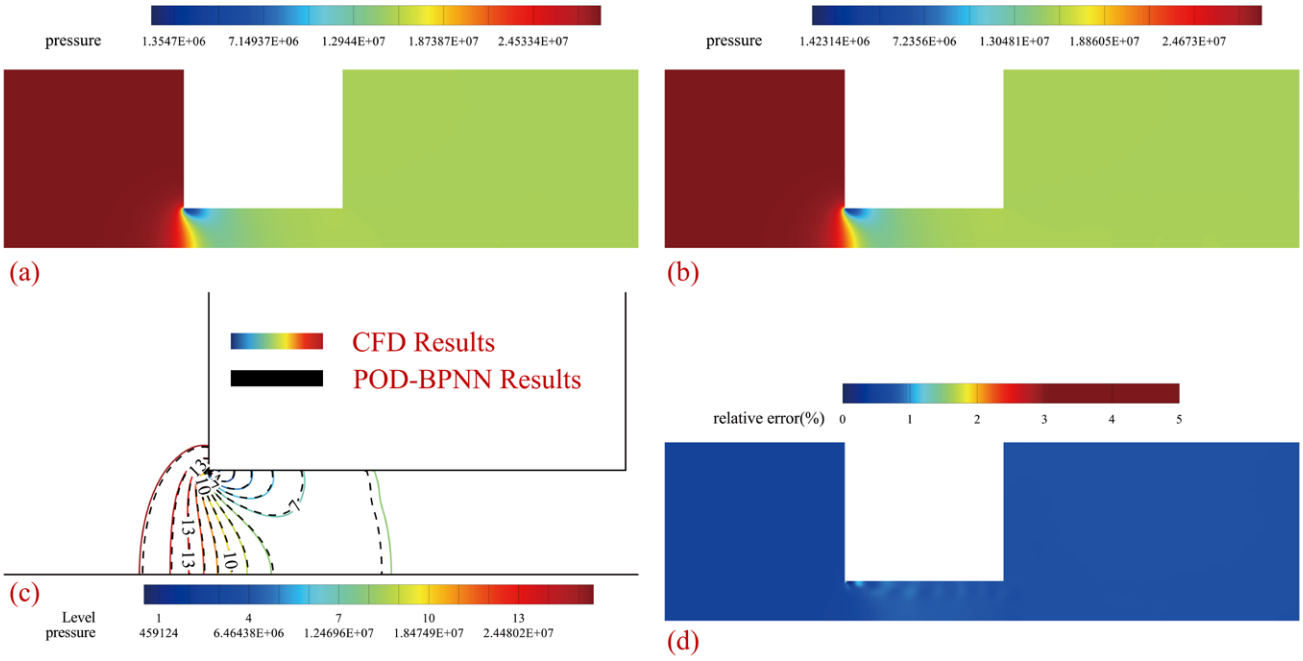

Fig. 18 Results of sample 7

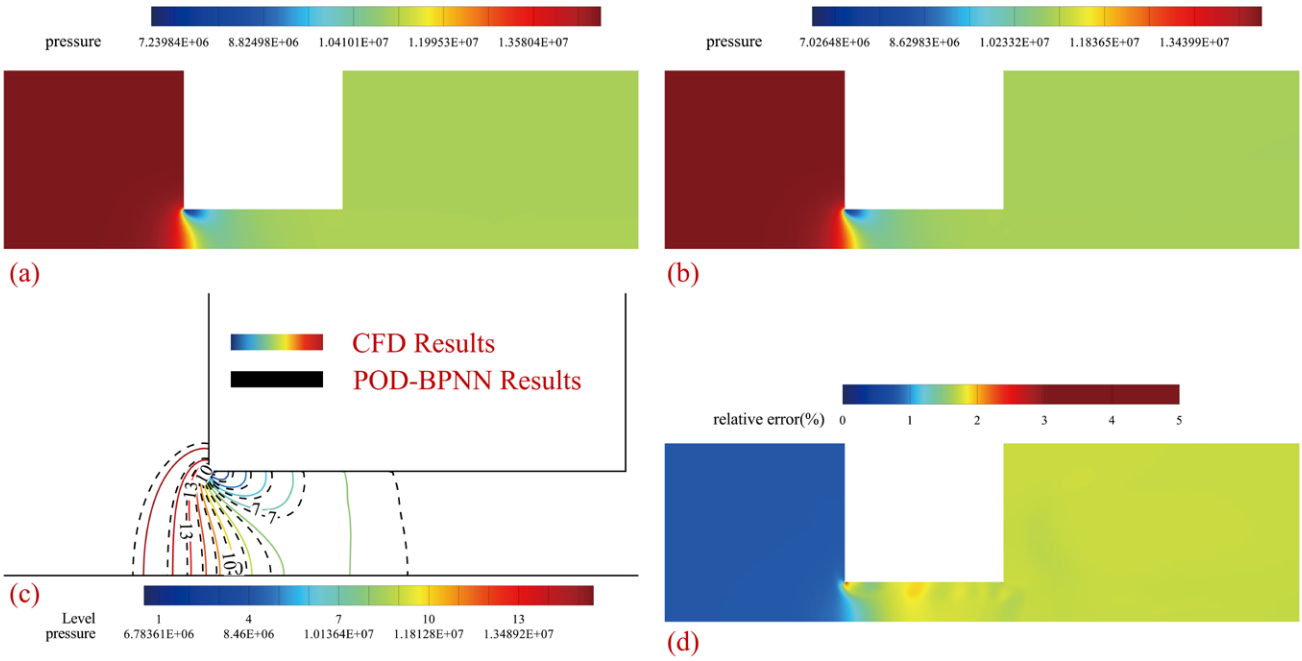

Fig. 19 Results of sample 8

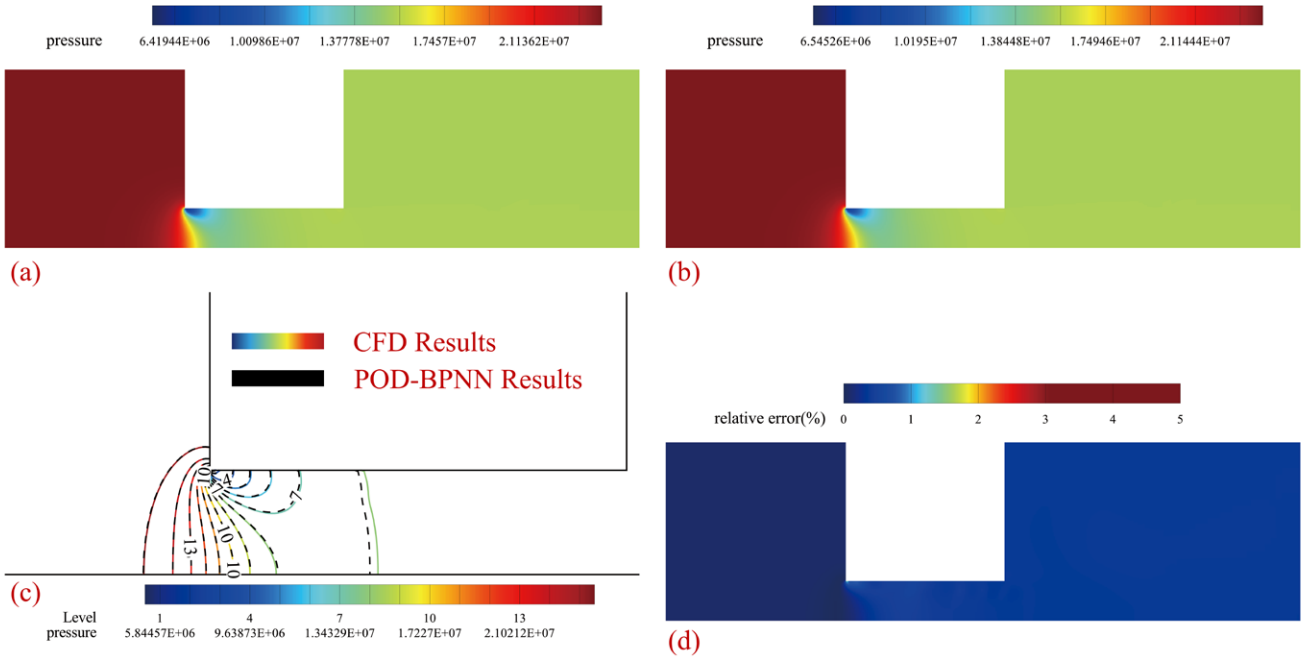

Fig. 20 Results of sample 9

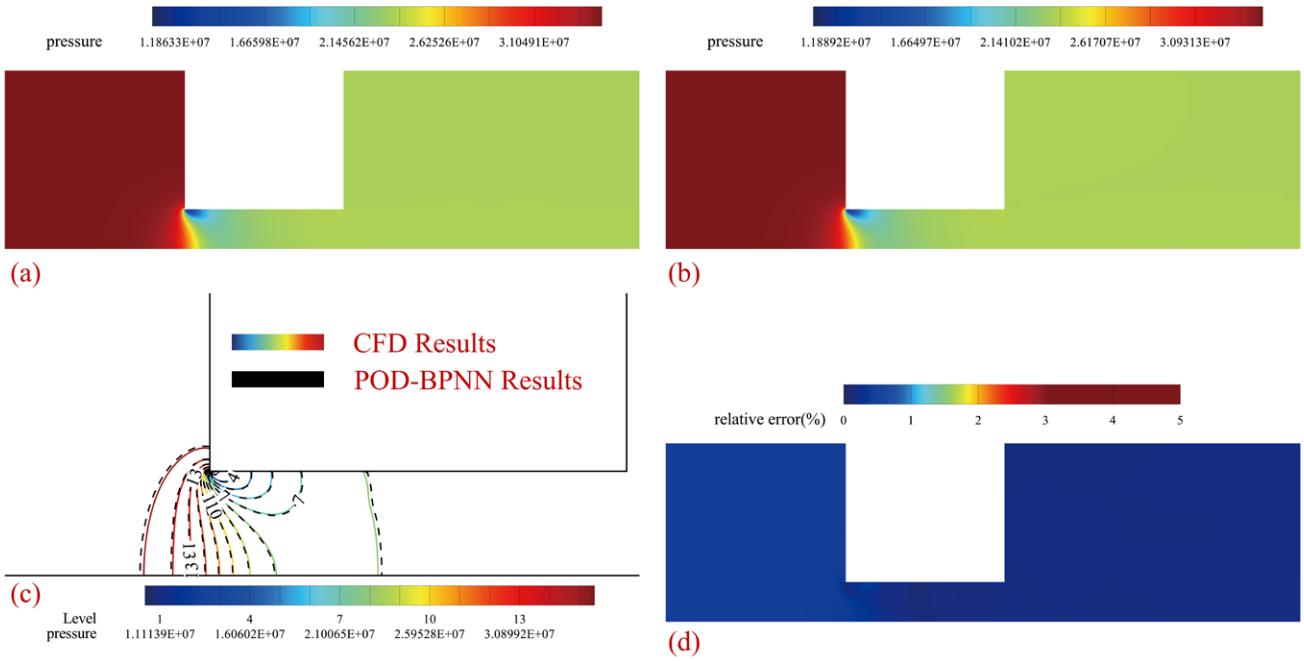

Fig. 21 Results of sample 10

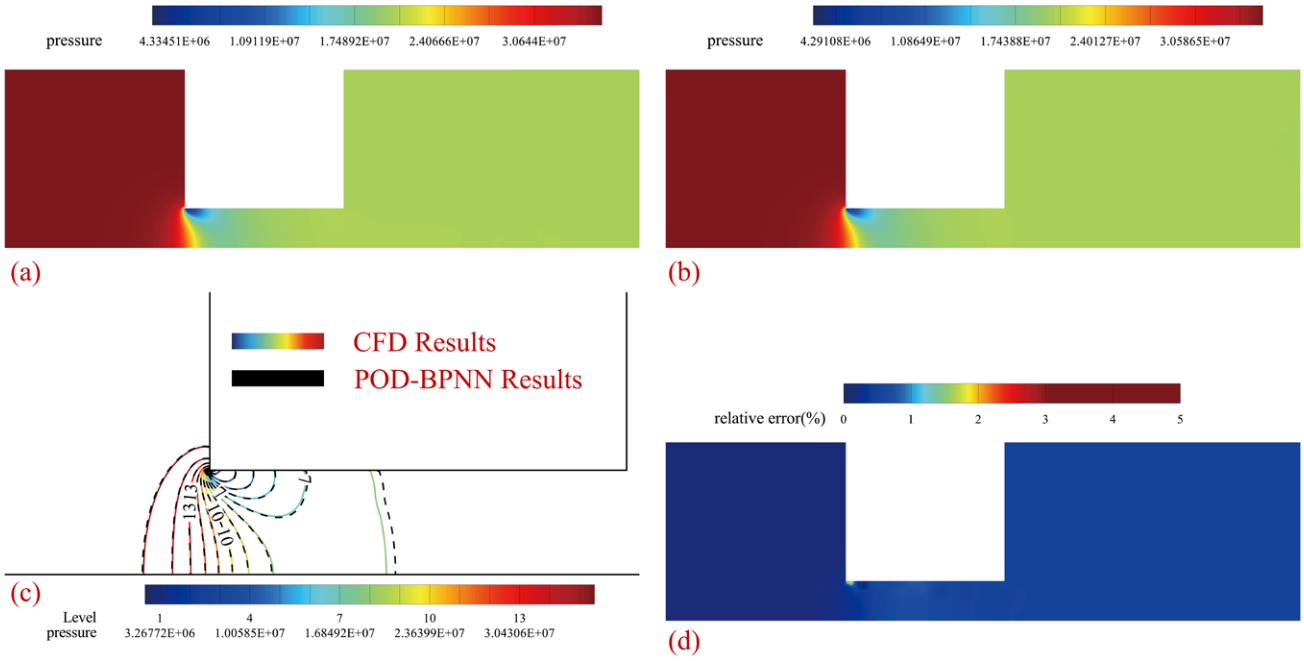

Fig. 22 Results of sample 11

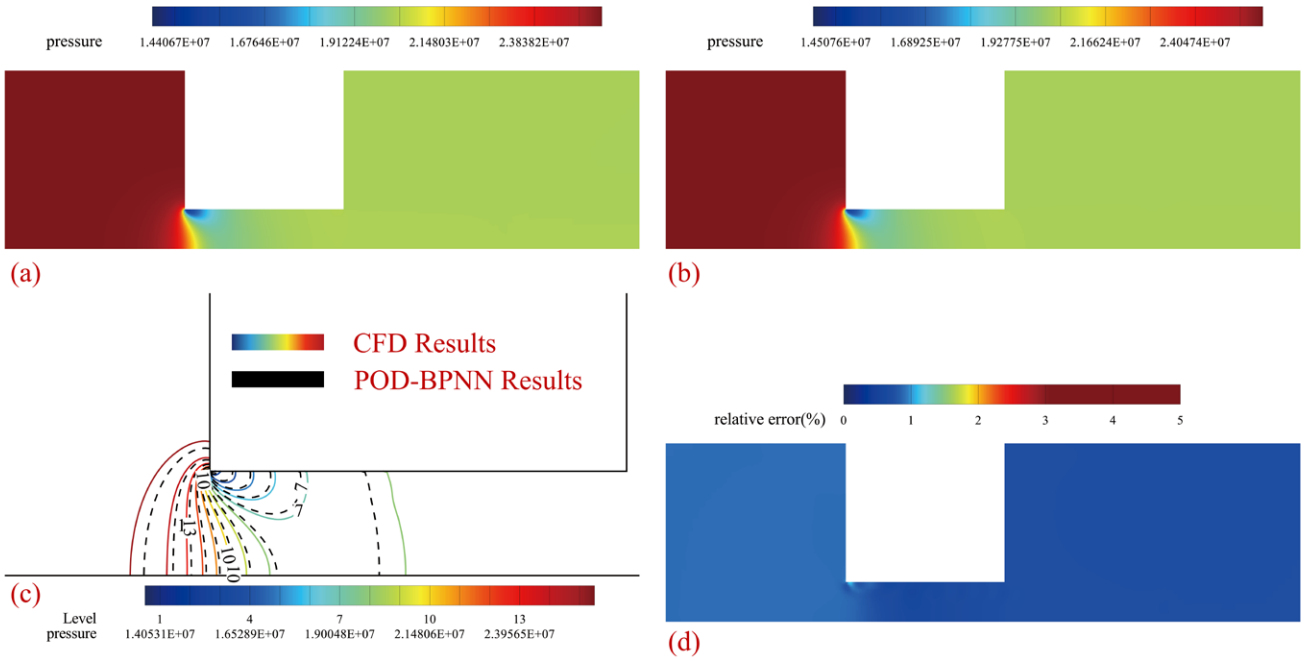

Fig. 23 Results of sample 12

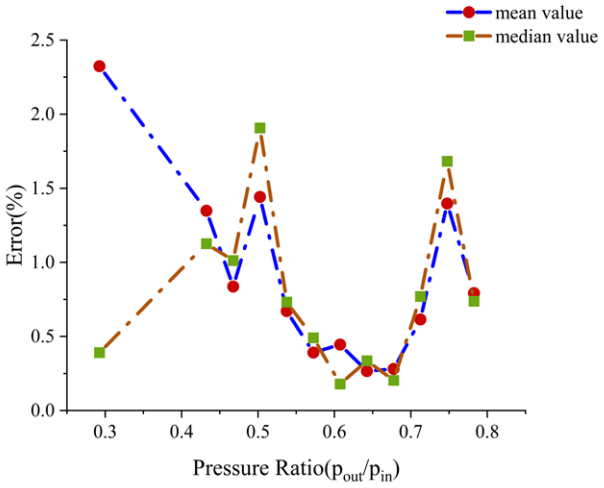

Fig. 24 The Trend of Error with Respect to Pressure Ratio

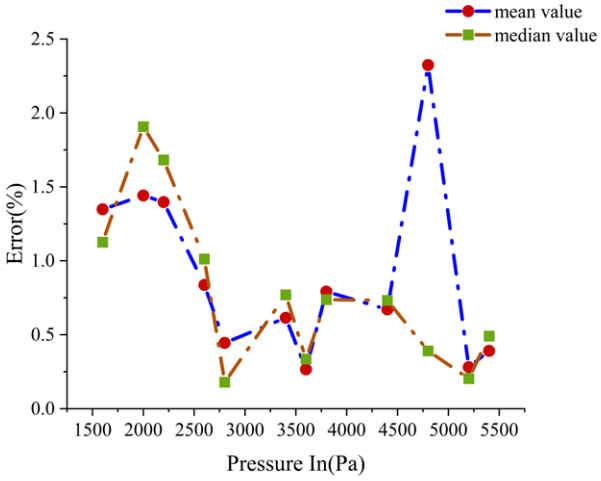

Fig. 25 The Trend of Error with Respect to Pressure In

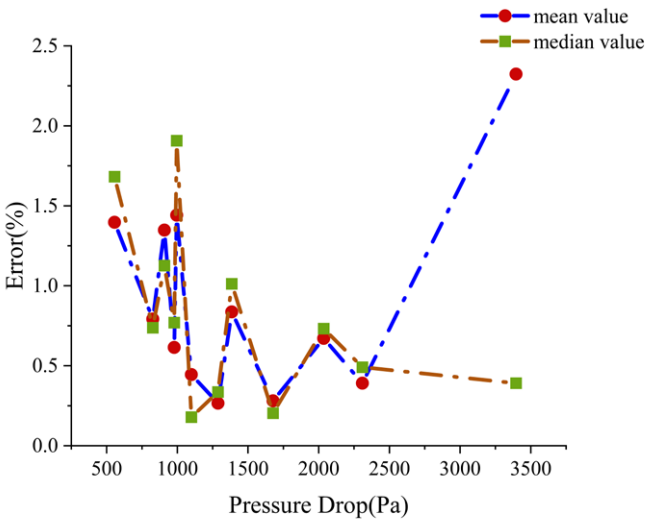

Fig. 26 The Trend of Error with Respect to Pressure Drop

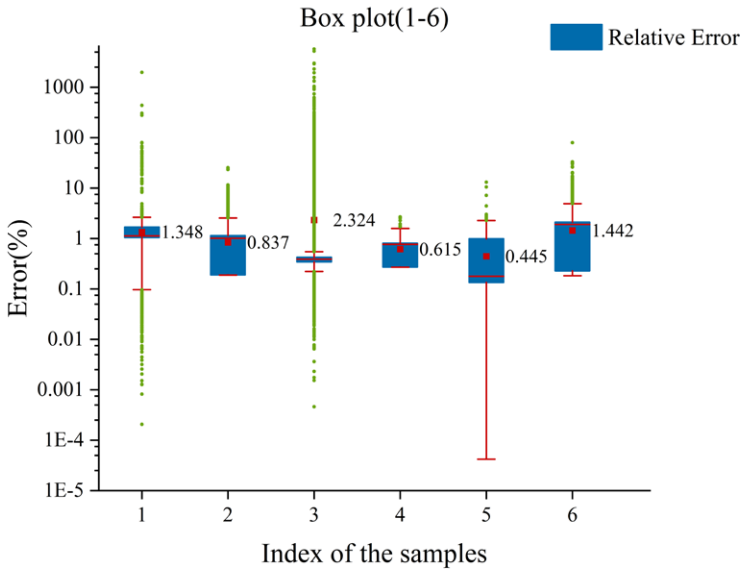

Fig. 27 Boxplot of the relative errors(sample 1-6)

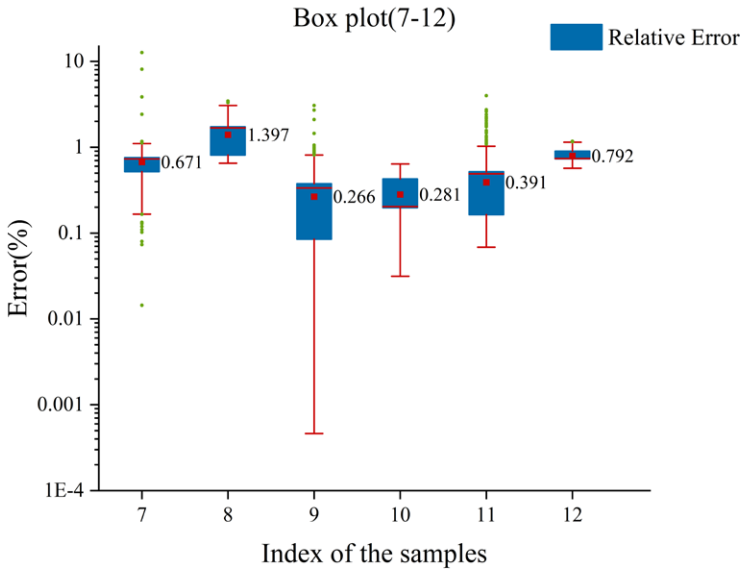

Fig. 28 Boxplot of the relative errors(sample 7-12)

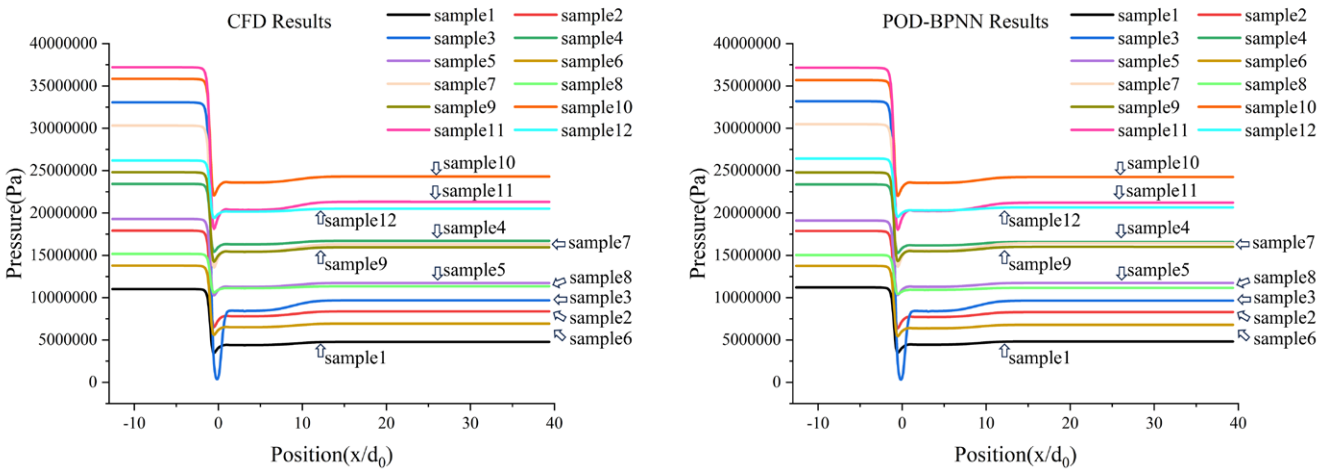

Fig. 29 CFD and POD-BPNN results of axial pressure distribution for the 12 samples

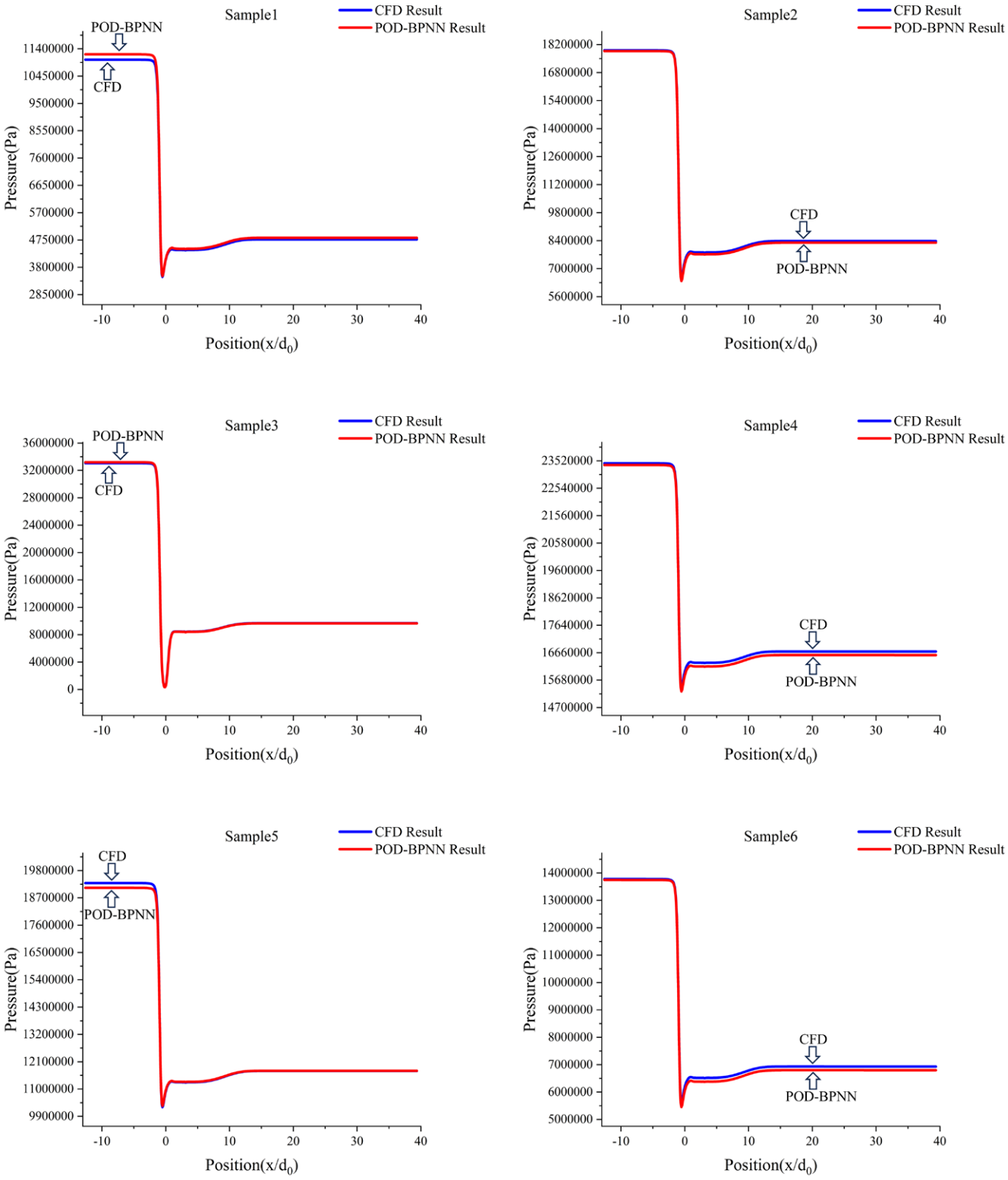

Fig. 30 Comparison of CFD results and POD-BPNN results for axial pressure distribution(sample 1-6)

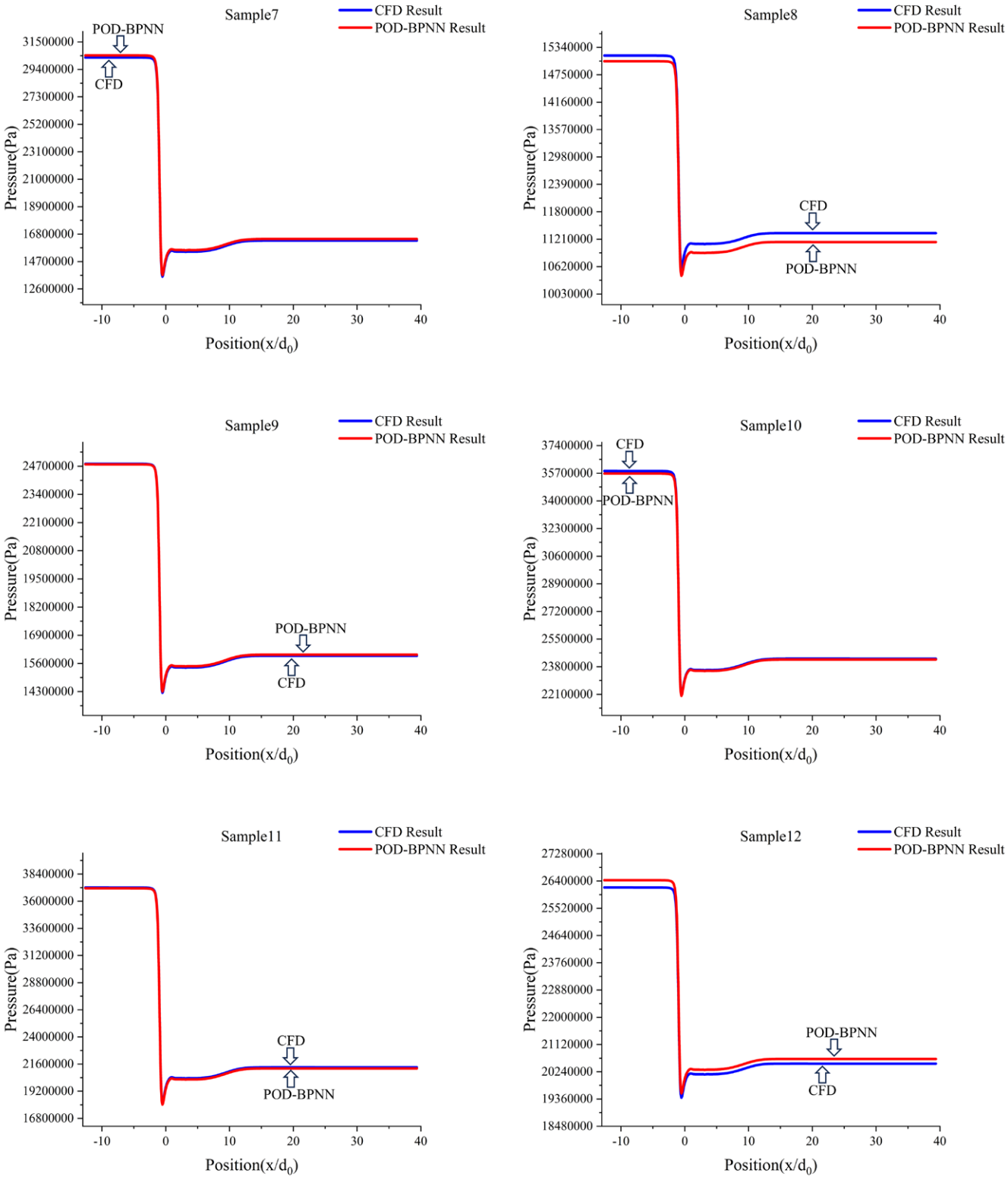

Fig. 31 Comparison of CFD results and POD-BPNN results for axial pressure distribution(sample7-12)

TABLE 1 OTHER SIMULATION PARAMETER SETTINGS

Name	Setting
turbulence model	standard $k-\omega$
multiphase flow model	mixture
cavitation model	Schnerr-Sauer
solution algorithm	coupled
gradient discretization	Least Squares Cell-Based
pressure discretization	PRESTO!
momentum discretization	Second Order Upwind
turbulent einetic energy discretization	First Order Upwind
specific dissipation rate discretization	First Order Upwind

TABLE 2 VALUES OF THE SAMPLES FOR TESTING

Sample Index	Pressure Outlet, psi	Pressure Inlet, psi	Ratio
1	1600	692	0.4325
2	2600	1215.5	0.4675
3	4800	1404	0.2925
4	3400	2422.5	0.7125
5	2800	1701	0.6075
6	2000	1005	0.5025
7	4400	2365	0.5375
8	2200	1644.5	0.7475
9	3600	2313	0.6425
10	5200	3523	0.6775
11	5400	3091.5	0.5725
12	3800	2973.5	0.7825

TABLE 3 VALUES OF SOME SAMPLES

Pressure Inlet, psi	Pressure Outlet, psi	Pressure Ratio
3438	2590.3611	0.75345
4790	3277.0785	0.68415
4714	756.8327	0.16055
4258	1914.6097	0.44965
5286	874.5687	0.16545
5450	2198.8025	0.40345
3834	1533.4083	0.39995
	……	

TABLE 4 STATISTICAL DISTRIBUTION OF RELATIVE ERRORS ACROSS 12 TEST SAMPLES

index	Mean Value	Standard Deviation	Median Value	Lower Quartile	Upper Quartile
1	1.348	8.897	1.126	1.050	1.685
2	0.837	0.647	1.012	0.190	1.138
3	2.324	45.112	0.391	0.344	0.425
4	0.615	0.251	0.770	0.272	0.808
5	0.445	0.423	0.179	0.135	0.991
6	1.442	1.066	1.907	0.229	2.105
7	0.671	0.130	0.732	0.520	0.756
8	1.397	0.430	1.682	0.810	1.732
9	0.266	0.140	0.336	0.085	0.376
10	0.281	0.108	0.204	0.198	0.428
11	0.391	0.173	0.491	0.164	0.518
12	0.792	0.084	0.738	0.734	0.902

TABLE 5 TIME CONSUMPTION OF THE CFD METHOD AND THE POD-BPNN METHOD

Method	Time Cost(s)											
CFD	840	960	720	840	840	720	960	720	840	900	900	780
POD-BPNN	0.0499	0.1395	0.0076	0.0079	0.0086	0.0091	0.0091	0.0085	0.0078	0.0072	0.0081	0.0091

[5] M. S. Shah, J. B. Joshi, A. S. Kalsi, C. S. R. Prasad, and D. S. Shukla, "Analysis of flow through an orifice meter: CFD simulation," *Chem. Eng. Sci.*, vol. 71, pp. 300–309.

[6] V. K. Singh and T. John Tharakan, "Numerical simulations for multi-hole orifice flow meter," *Flow Meas. Instrum.*, vol. 45, pp. 375–383, Oct. 2015.

[7] M. M. Tukiman *et al.*, "CFD simulation of flow through an orifice plate," *IOP Conf. Ser. Mater. Sci. Eng.*, vol. 243, no. 1, p. 012036, Sep. 2017.

[8] B. Ebrahimi *et al.*, "Characterization of high-pressure cavitating flow through a thick orifice plate in a pipe of constant cross section," *Int. J. Therm. Sci.*, vol. 114, pp. 229–240.

[9] X. Li, B. Huang, T. Chen, Y. Liu, S. Qiu, and J. Zhao, "Combined experimental and computational investigation of the cavitating flow in an orifice plate with special emphasis on surrogate-based optimization method," *J. Mech. Sci. Technol.*, vol. 31, no. 1, pp. 269–279.

[10] J. Zhang, Q. Du, and Y. Yang, "Influence of diesel nozzle geometry on cavitation using eulerian multi-fluid method," *Trans. Tianjin Univ.*, vol. 16, no. 1, pp. 33–39, Feb. 2010.

[11] Y. Zhang, J. Lai, C. He, and S. Yang, "Cavitation optimization of single-orifice plate using CFD method and neighborhood cultivation genetic algorithm," *Nucl. Eng. Technol.*, vol. 54, no. 5, pp. 1835–1844, May 2022.

[12] F. Chen *et al.*, "Predicting roof-surface wind pressure induced by conical vortex using a BP neural network combined with POD," *Build. Simul.*, vol. 15, no. 8, pp. 1475–1490.

[13] H. Dongmei, H. Shiqing, H. Xuhui, and Z. Xue, "Prediction of wind loads on high-rise building using a BP neural network combined with POD," *J. Wind Eng. Ind. Aerodyn.*, vol. 170, pp. 1–17, Nov. 2017.

[14] J. S. Hesthaven and S. Ubbiali, "Non-intrusive reduced order modeling of nonlinear problems using neural networks," *J. Comput. Phys.*, vol. 363, pp. 55–78, Jun. 2018.

[15] S. Miah, Y. Sooriyakanthan, P. D. Ledger, A. J. Gil, and M. Mallett, "Reduced order modelling using neural networks for predictive modelling of 3d-magneto-mechanical problems with application to magnetic resonance imaging scanners," *Eng. Comput.*, vol. 39, no. 6, pp. 4103–4127, 2023.

[16] G. Min and N. Jiang, "Flow fields prediction for data-driven model of parallel twin cylinders based on POD-RBFNN and POD-BPNN surrogate models," *Ann. Nucl. Energy*, vol. 199, p. 110342, May 2024.

[17] K. Wang *et al.*, "Rapid reconstruction of temperature field of coke chamber based on POD-BP and Tikhonov method," *Therm. Sci.*, vol. 27, no. 5 Part A, pp. 3513–3524, 2023.

[18] G. Min and N. Jiang, "Data-driven identification and pressure fields prediction for parallel twin cylinders based on POD and DMD method," *Phys. Fluids*, vol. 36, no. 2, p. 023614, Feb. 2024.

[19] Warjito, Budiarso, and Dendy Adanta, "Computational Analysis of Flow Field on Cross-Flow Hydro Turbines," Engineering Letters, vol. 29, no.1, pp87-94, 2021

[20] M. D. McKay, W. J. Conover, and D. E. Whiteman, "Report on the application of statistical techniques to the analysis of computer codes," Los Alamos National Lab. (LANL), Los Alamos, NM (United States), LA-6479-MS, Aug. 1976.

[21] F. Sun, G. Xie, J. Song, and C. N. Markides, "Proper orthogonal decomposition and physical field reconstruction with artificial neural networks (ANN) for supercritical flow problems," *Eng. Anal. Bound. Elem.*, vol. 140, pp. 282–299, Jul. 2022.

[22] L. Sirovich, "Turbulence and the dynamics of coherent structures. I. Coherent structures," *Q. Appl. Math.*, vol. 45, no. 3, pp. 561–571, 1987.

Xing Hu has completed his Bachelor's degree from Sichuan University in Chengdu, Sichuan, China, and is currently pursuing a Master's degree at the same institution. His research interests are focused on digital twin technology and mechatronics engineering.

Ruiping Xiong currently holds the position of Associate Professor at Sichuan University. He has obtained his Bachelor's, Master's, and Ph.D. degrees from the same institution. His research interests are centered on industrial robotics, digital twin technology, and mechatronics engineering.

Zhongping Zhao has completed his Bachelor's degree from Sichuan University in Chengdu, Sichuan, China, and is currently pursuing a Master's degree at the same institution. His research interests are focused on computational fluid dynamics and mechatronics engineering.

Junhong Yang has completed his Bachelor's degree from Sichuan University in Chengdu, Sichuan, China, and is currently pursuing a Master's degree at the same institution. His research interests are focused on industrial robotics path planning and mechatronics engineering.